

NEUROPHYSIOLOGY

Dendritic and parallel processing of visual threats in the retina control defensive responses

T. Kim^{1,2*}, N. Shen¹, J.-C. Hsiang^{1,2}, K.P. Johnson^{1,2}, D. Kerschensteiner^{1,3,4,5†}

Approaching predators cast expanding shadows (i.e., looming) that elicit innate defensive responses in most animals. Where looming is first detected and how critical parameters of predatory approaches are extracted are unclear. In mice, we identify a retinal interneuron (the VG3 amacrine cell) that responds robustly to looming, but not to related forms of motion. Looming-sensitive calcium transients are restricted to a specific layer of the VG3 dendrite arbor, which provides glutamatergic input to two ganglion cells (W3 and OFF α). These projection neurons combine shared excitation with dissimilar inhibition to signal approach onset and speed, respectively. Removal of VG3 amacrine cells reduces the excitation of W3 and OFF α ganglion cells and diminishes defensive responses of mice to looming without affecting other visual behaviors. Thus, the dendrites of a retinal interneuron detect visual threats, divergent circuits downstream extract critical threat parameters, and these retinal computations initiate an innate survival behavior.

INTRODUCTION

To survive, animals need to evade threats in their environments. How sensory systems detect threats quickly and how they measure critical parameters of a threat (e.g., the speed of an approaching predator) to select appropriate behavioral responses are central questions in neuroscience. Approaching objects cast expanding shadows (i.e., looming) that elicit innate defensive reactions in a wide range of animals, from insects to humans (1, 2). Mice use vision to avoid aerial predators (3, 4). The midbrain circuits that mediate looming responses in mice have been studied extensively (5–10), but where looming-selective signals first arise and how crucial parameters of predatory approaches are computed are unclear.

Early investigators suggested that the retina detects specific stimulus features and signals them to the brain through ganglion cell spike trains to trigger rapid behavioral responses (11, 12). Since then, a wide range of feature-selective responses has been identified in approximately 40 retinal ganglion cell types of mammals (13, 14). However, except for a link between direction-selective responses and a gaze-stabilizing reflex (15, 16), the behavioral significance of retinal feature detection remains uncertain. Furthermore, behavioral salience often depends on a combination of stimulus features (17). Whether and how the retina generates cooperative feature representations in ganglion cells are unknown.

The stimulus preferences of ganglion cells are shaped by amacrine cells, a diverse class of interneurons that encompasses more than 60 cell types (18–20). In part because of this diversity, the organization and function of circuits between amacrine and ganglion cells are poorly understood, a state that is emblematic of interneuron circuits throughout the nervous system (18, 21).

¹John F. Hardesty, MD Department of Ophthalmology and Visual Sciences, Washington University School of Medicine, St. Louis, MO 63110, USA. ²Graduate Program in Neuroscience, Washington University School of Medicine, Saint Louis, MO 63110, USA. ³Department of Neurosciences, Washington University School of Medicine, Saint Louis, MO 63110, USA. ⁴Department of Biomedical Engineering, Washington University School of Medicine, Saint Louis, MO 63110, USA. ⁵Hope Center for Neurological Disorders, Washington University School of Medicine, Saint Louis, MO 63110, USA.

*Present address: Janelia Research Campus, Howard Hughes Medical Institute, Ashburn, VA 20147, USA.

†Corresponding author. Email: kerschensteinerd@wustl.edu

Most amacrine cells lack axons and receive input and provide output through their dendrites (18). By restricting the spread of input signals, different amacrine cell dendrites can compute different visual information and convey this information to separate targets (18, 22, 23). This enhances the computational power of amacrine cells and the complexity of retinal circuits. The sensory computations of amacrine cell dendrites, their influence on feature representations of ganglion cells, and contributions to vision are mostly unknown.

Here, we combine two-photon guided patch-clamp recordings, dendritic calcium imaging, optogenetics, anatomical circuit reconstructions, type-specific cell deletion, and behavioral assays to decipher the retinal processing of visual threats and its contributions to defensive responses.

RESULTS

Behavioral and neuronal responses to looming

We presented dark expanding disks (i.e., looming) on a monitor above a rectangular arena with virtual shelters on two sides (Fig. 1A; see Materials and Methods). After a period of acclimatization (>5 min), looming was triggered when mice crossed the center of the arena. Looming elicited stereotypic responses in which mice fled to a shelter and froze (Fig. 1, A and D, and movie S1). Consistent with previous observations (3), neither receding (i.e., dark contracting disks) nor white looming evoked similar responses (Fig. 1, B to D, and movies S2 and S3). How retinal circuits process looming and distinguish it from related forms of motion and which retinal circuits drive defensive behaviors are unclear.

Amacrine cells are an extraordinarily diverse class of interneurons that enable the retina to distinguish different forms of motion (18–20, 24, 25). On the basis of their receptive field properties (22, 23, 26, 27), we hypothesized that VGLUT3-expressing (VG3) amacrine cells contribute to the retinal processing of looming. In targeted patch-clamp recordings, we found that VG3 amacrine cells depolarized strongly to looming (Fig. 1, E and H, and fig. S1), hyperpolarized to receding (Fig. 1, F and H), and responded weakly to white looming (Fig. 1, G and H). In voltage-clamp recordings, excitatory inputs elicited by looming were consistently faster than those elicited by white looming (Fig. 1, I, K, and L). This created a window during which excitation exceeded inhibition, explaining the greater

Copyright © 2020
The Authors, some
rights reserved;
exclusive licensee
American Association
for the Advancement
of Science. No claim to
original U.S. Government
Works. Distributed
under a Creative
Commons Attribution
NonCommercial
License 4.0 (CC BY-NC).

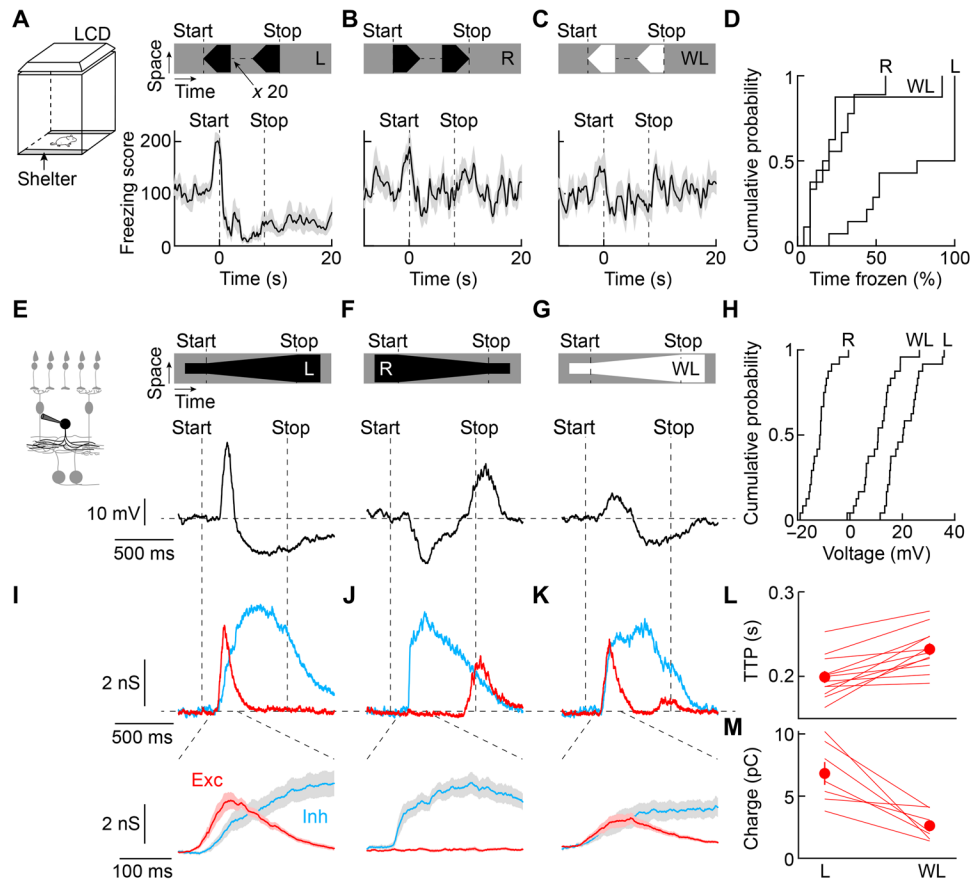


Fig. 1. Behavioral and neuronal looming responses. (A to C) Visual stimuli were shown to mice in a behavioral arena with virtual shelters (i.e., areas in which the monitor remained dark) on two sides. Freezing score responses of wild-type mice to looming (A; $n = 14$ mice), receding (B; $n = 9$ mice), and white looming (C; $n = 8$ mice). Lines (shaded areas) indicate mean (\pm SEM). LCD, liquid-crystal display. (D) Cumulative distributions of the time mice spent frozen from stimulus onset to 20 s later (stimulus duration: 8 s) for looming (L), receding (R), and white looming (WL). L versus R: $P = 0.0033$; L versus WL: $P = 0.0028$; R versus WL: $P = 0.99$; Kruskal-Wallis test. (E to G) Representative voltage traces of VG3-ACs (VG3-Cre Ai9 mice) during looming (E), receding (F), and white looming (G). Throughout this figure, the stimulus speed was $800 \mu\text{m s}^{-1}$. (H) Cumulative distributions of VG3 voltage responses to looming (L), receding (R), and white looming (WL). For all stimuli, $n = 24$ cells. L versus R: $P = 9.7 \times 10^{-10}$; L versus WL: $P = 0.0015$; R versus WL: $P = 0.0015$; Friedman's test with Tukey-Kramer post hoc analysis. (I to K) Bottom traces show representative excitatory and inhibitory inputs to looming (I), receding (J), and white looming (K). Top traces (shaded areas) depict the mean (\pm SEM) responses starting 100 ms after the onset of motion. (L and M), Summary data comparing the time to peak (TTP) of excitation (L; $n = 12$ cells, $P = 4.8 \times 10^{-4}$, Wilcoxon signed-rank test) and the charge transferred during the window while excitation exceeds inhibition (M; $n = 7$ cells, $P = 0.016$, Wilcoxon signed-rank test).

depolarization of VG3 amacrine cells to looming than white looming (Fig. 1, I, K, and M). Receding elicited strong synaptic inhibition with excitation relegated to the stimulus offset (Fig. 1J).

Dendritic processing of looming in VG3 amacrine cells

Amacrine cells send and receive signals through their dendrites. Thus, one amacrine cell can contain multiple input-output pathways that process information separately, bypassing the soma (22, 23, 28, 29). We used two-photon calcium imaging to analyze motion signals in VG3 dendrite arbors. Looming elicited robust calcium transients in VG3 dendrites in the outer part of the inner plexiform layer (Fig. 2, A and D). By contrast, receding did not evoke calcium transients during motion (Fig. 2, B and D), and the preference for looming versus receding was high throughout the VG3 dendrite arbor (Fig. 2E and fig. S2). White looming signals were weak and restricted to VG3 dendrites in the inner part of the inner plexiform layer (Fig. 2, C and D). Throughout the VG3 arbor, the preference for looming versus white looming was greater than the preference for stationary dark

versus bright stimuli (Fig. 2F and fig. S2), and the preference for looming versus white looming in calcium signals was greater than that observed in voltage recordings (calcium, 0.75 ± 0.04 ; voltage, 0.35 ± 0.06 ; $P = 8.92 \times 10^{-7}$). Thus, looming-sensitive calcium signals are enhanced by dendritic nonlinearities and spatially segregated from weaker responses to related forms of motion.

VG3 amacrine cells provide excitatory input to W3 and OFF α ganglion cells

The VG3 dendrites with the most robust looming responses overlap with the dendrites of two ganglion cell types that have been suggested to signal approaching aerial predators: W3 and OFF α (30–32). We used optogenetics to test the functional connectivity of VG3 amacrine cells with W3 and OFF α ganglion cells. VG3 amacrine cells are dual transmitter neurons that release glutamate and glycine (33, 34). We pharmacologically blocked transmission of photoreceptor signals to bipolar cells and matched Channelrhodopsin-2-mediated depolarizations of VG3 amacrine cells to their physiologic light responses

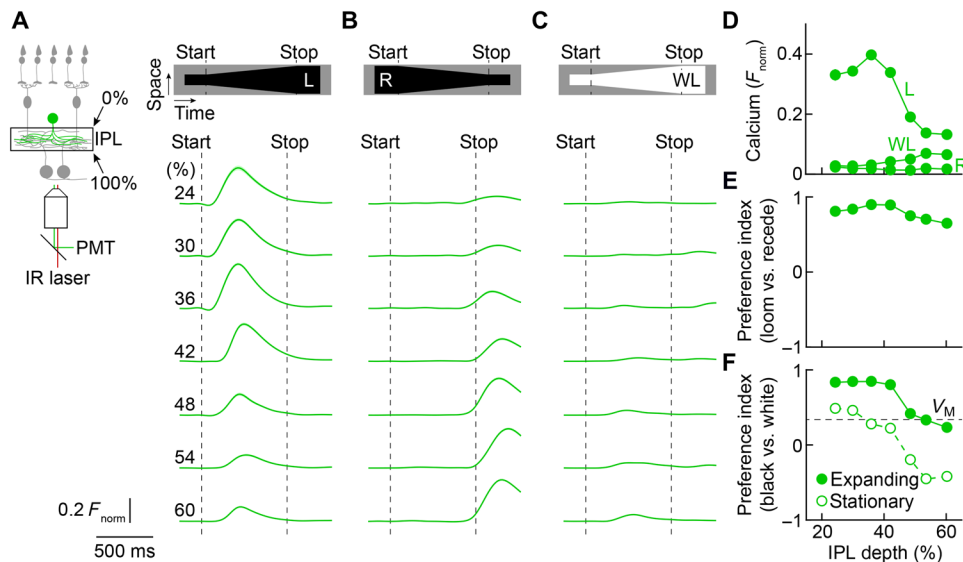


Fig. 2. Dendritic processing of visual stimuli in VG3 amacrine cells. (A to C) Two-photon imaging of calcium transients in VG3 dendrites (VG3-Cre *Ai148* mice) during looming (A), receding (B), and white looming (C). IR, infrared; PMT, photomultiplier tube. Green traces indicate the mean (shaded areas, almost indistinguishable from the green lines, indicate \pm SEM) responses of dendritic regions of interest (ROIs) at different depths of the inner plexiform layer (IPL; 24%: $n = 68$ ROIs; 30%: $n = 138$ ROIs; 36%: $n = 137$ ROIs; 42%: $n = 153$ ROIs; 48%: 163 ROIs; 54%: $n = 162$ ROIs; 60%: $n = 329$ ROIs). (D) Average (\pm SEM) response amplitudes plotted as a function of IPL depth. Error bars indicating SEM are not visible because they are smaller than the circles. For IPL depths, 24 to 36% R and WL responses were not significantly different ($P > 0.11$); all other responses at all IPL depths were significantly different ($P < 3.3 \times 10^{-9}$, Friedman's test with Tukey-Kramer post hoc analysis). (E and F) Summary data (means \pm SEM) of preference indices for looming versus receding (E) and black versus white stimuli (F; expanding: filled circles; stationary: empty circles) across IPL depths. Error bars indicating SEM are not visible because they are smaller than the circles. For the preference index for looming versus receding (E), $P = 1.3 \times 10^{-21}$ for the main effect of IPL depth, Kruskal-Wallis test. By Tukey-Kramer post hoc analysis, pairwise comparisons showed statistically significant differences ($P < 0.02$) for 24 versus 54% and versus 60%, for 30 versus 48 to 60%, for 36 versus 48 to 60%, and for 42 versus 48 to 60%. For the preference index for looming versus white looming (F), $P = 0$ for the main effect of IPL depth, Kruskal-Wallis test. By Tukey-Kramer post hoc analysis, all pairwise comparisons revealed statistically significant differences ($P < 0.02$) except for 24 versus 30 to 42%, for 30 versus 36% and versus 42%, for 36 versus 42%, and for 54 versus 60%. For the preference index for black versus white stationary (F), $P = 0$ for the main effect of IPL depth, Kruskal-Wallis test. By Tukey-Kramer post hoc analysis, all pairwise comparisons revealed statistically significant differences ($P < 0.02$) except for 24 versus 30% and versus 36%, for 30 versus 36%, for 36 versus 42%, and for 54 versus 60%. At all depths, the preference index for black versus white looming was greater than that for stationary stimuli ($P = 0$ for a comparison across all depths and $P < 10^{-9}$ for comparisons at each depth, Wilcoxon signed-rank test). In (F), the preference index for looming versus white looming for voltage responses (V_M) is shown by a dashed line.

(33). Optogenetic activation of VG3 amacrine cells elicited postsynaptic currents that reversed near 0 mV (Fig. 3, A and B), the reversal potential for cation-nonspecific conductances in our recording conditions, in W3 and OFF α ganglion cells, indicating that VG3 amacrine cells provide purely glutamatergic input to both targets (27, 35).

To reconstruct anatomical connectivity patterns, we biolistically labeled OFF α ganglion cells with cytosolic cyan fluorescent protein and PSD95–yellow fluorescent protein (YFP), a marker of excitatory synapses (36), in mice in which VG3 amacrine cells express tdTomato (VG3-Cre *Ai9*; Fig. 3, C and D). In confocal image stacks, we found that approximately half the PSD95–YFP clusters on OFF α dendrites were apposed by VG3 boutons (Fig. 3E). The number of appositions markedly dropped when we rotated the tdTomato channel by 90° (Fig. 3E). Using a similar approach, we previously found that VG3 dendrites account for approximately half the excitatory synapses on W3 dendrites (26). Thus, VG3 amacrine cells provide a similar fraction ($\sim 1/2$) of the excitatory input to W3 and OFF α ganglion cells.

Parallel parameter estimation in divergent VG3 circuits

To understand how looming signals are transformed from VG3 amacrine cells to W3 and OFF α ganglion cells, we analyzed the responses and underlying synaptic inputs of all three cells to dark disks expanding at different speeds. Responses of VG3 amacrine cells were restricted to the onset of motion (stimulus size at peak: $145 \pm 8 \mu\text{m}$,

$4.3 \pm 0.2^\circ$, $n = 24$ cells) and stable across looming speeds (Fig. 4, A and B). Responses were restricted to the onset of motion because transient excitation preceded sustained inhibition (Fig. 4, C and E). Responses were stable across looming speeds because the amplitudes of excitation and inhibition increased in parallel with stimulus speed, maintaining balance (Fig. 4D). W3 ganglion cells received a similar sequence of synaptic excitation and inhibition. Both inputs increased in amplitude together as a function of stimulus speed (Fig. 4, H to J). W3 ganglion cell responses, therefore, similar to those of VG3 amacrine cells, signaled the onset (i.e., critical size) of looming (stimulus size at peak: $154 \pm 12 \mu\text{m}$, $4.5 \pm 0.4^\circ$, $n = 5$ cells) stably across different speeds of expansion (Fig. 4, F and G). By contrast, OFF α ganglion cell responses increased during looming motion and increased at higher stimulus speeds (Fig. 4, K and L) (31). Responses increased during motion because excitation coincided with disinhibition (Fig. 4, M and O). Responses increased at higher speeds as excitation and inhibition diverged in amplitudes (Fig. 4N). Stimulation with stationary dark spots revealed that the cell type–specific trajectories of excitation and inhibition during looming were temporal realizations of distinct receptive field architectures by expanding motion (Fig. 4, E, J, and O, and fig. S3). W3 and OFF α ganglion cells strongly preferred expanding over contracting motion (fig. S4). Thus, by combining similar and, in part, shared excitatory input with dissimilar inhibition W3 and OFF α ganglion cells, which form

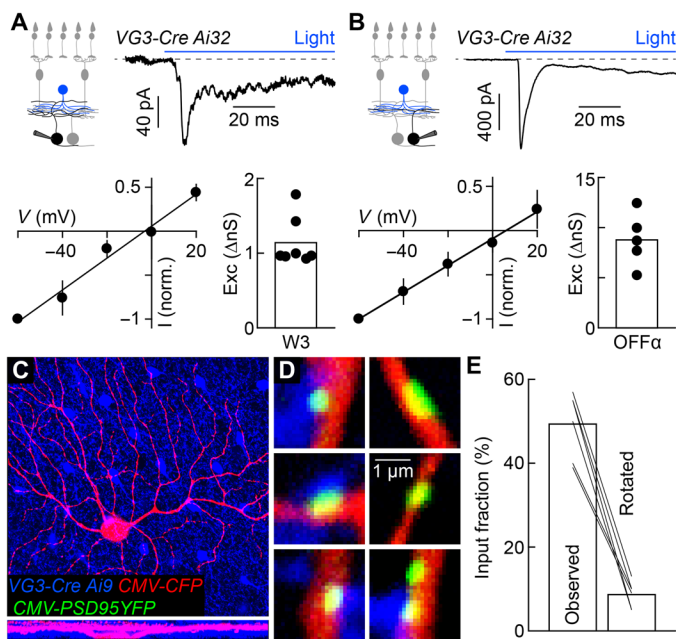


Fig. 3. VG3 amacrine cells provide excitatory synaptic input to W3 and OFF α ganglion cells. (A and B) Optogenetic stimulation of VG3 amacrine cells (*VG3-Cre Ai32* mice) elicits postsynaptic currents in W3 (A; $n = 7$ cells) and OFF α (B; $n = 5$ cells) ganglion cells. Reversal near 0 mV identifies these as excitatory postsynaptic currents (EPSCs). (C and D) Overview projections (C) and single-plane excerpts (D) of a confocal image stack of an OFF α cell biolistically labeled with cyan fluorescent protein (CFP; C and D) and PSD95-YFP (D) in a retina, in which VG3 amacrine cells express tdTomato (*VG3-Cre Ai9* mice). (E) Summary data of the fraction of PSD95-YFP puncta apposed by VG3 boutons in the obtained image stacks (observed) or the tdTomato channel was rotated by 90° (rotated, $n = 6$ cells; observed versus rotated: $P = 0.03$ by Wilcoxon signed-rank test). Exc, excitation; I, current; V, voltage.

parallel pathways from the retina to the brain, transform signals from VG3 amacrine cells to encode the onset (i.e., critical size) and speed of looming, respectively.

Responses of W3 and OFF α ganglion cells to looming depend on VG3 amacrine cells

To test the contributions of VG3 amacrine cells to the looming responses of W3 and OFF α ganglion cells, we selectively removed VG3 amacrine cells from the adult retina by injecting *VG3-DTR* mice intraperitoneally with diphtheria toxin (DT; fig. S5) (33, 35). We first analyzed the effect of this manipulation on ganglion cell dendrites and their synapses. Using biolistic labeling and confocal reconstructions, we found that VG3 removal did not affect the size of W3 and OFF α dendrite arbors but approximately halved the density of excitatory synapses (Fig. 5, A to D). This synapse loss matched the estimated fraction of excitatory synapses from VG3 amacrine cells in control retinas (Fig. 3E) (36), indicating that ganglion cells do not shift connections to other input partners in the adult retina as they do during development (37, 38).

In patch-clamp recordings, we found that the responses of W3 (Fig. 6, A to C) and OFF α ganglion cells (Fig. 6, D to F) to looming were attenuated by the removal of VG3 amacrine cells across a wide range of stimulus contrasts and speeds. For both ganglion cell types, this was caused by reduced synaptic excitation during looming (Fig. 6, G to L), whereas inhibition of W3 (Fig. 6, M and O) and disinhibition of OFF α

ganglion cells (Fig. 6, P and R) were unchanged. Thus, looming signals from the retina to the brain depend on VG3 amacrine cells.

Defensive responses to looming stimuli depend on VG3 amacrine cells

We next wanted to test how the removal of VG3 amacrine cells affects the behavioral responses to looming stimuli. In *VG3-DTR* mice, VG3 neurons in the retina and the brain express the DT receptor. Using tdTomato labeling in *VG3-DTR Ai9* mice as a proxy, we found that a subset of midbrain areas involved in defensive responses to looming contain VG3 neurons (fig. S5) (5–10). To our surprise, these neurons were unaffected by intraperitoneal injections of DT that ablated most VG3 amacrine cells (fig. S5). Thus, the systemic administration of DT selectively removed VG3 neurons in the retina. To ensure further that cell removal was restricted to the retina, we alternatively injected DT directly into both eyes (i.e., intraocularly) of *VG3-DTR* mice (fig. S5).

In behavioral experiments, we found that the stereotypic behavioral responses to looming consisting of flight and prolonged freezing were preserved in control mice injected with DT intraperitoneally (Fig. 7, A and C, and movie S4) or i.o. (Fig. 7, E and G, and movie S5) but diminished by the same injections in *VG3-DTR* mice (Fig. 7, B, C, F, and G, and movies S6 and S7). In contrast, all four groups of mice performed indistinguishably in a visual cliff test (Fig. 7, D and H). Furthermore, visually evoked potentials, which measure the signals propagated along the retino-geniculo-cortical pathway, were not significantly different between *VG3-DTR* mice and littermate controls irrespective of the DT injection site (Fig. 7, I to P). Thus, VG3 amacrine cells are required selectively for the innate defensive responses of mice to looming.

DISCUSSION

Threat detection and assessment are essential functions of nervous systems. Yet, where threats are detected and how critical threat parameters are measured to guide behavioral responses are unclear. Here, we characterize circuits in the mouse retina that process looming, a visual threat that elicits innate defensive responses in a wide range of animals, including humans (1, 2). We reach six main conclusions. First, a retinal interneuron (the VG3 amacrine cell) detects looming through stimulus-specific delays between synaptic excitation and inhibition. Second, the dendrites of VG3 amacrine cells enhance and spatially isolate looming signals. Third, the looming-sensitive dendrites of VG3 amacrine cells provide excitatory input to two ganglion cell types: W3 and OFF α . Fourth, W3 and OFF α ganglion cells combine shared excitation with dissimilar inhibition to encode the onset and speed of looming, respectively. Fifth, looming responses of W3 and OFF α ganglion cells depend on VG3 amacrine cells. Sixth, innate defensive responses to looming, but not other visual behaviors, depend on VG3 amacrine cells.

A contrast-specific delay in synaptic inputs generates feature selectivity

VG3 amacrine cells receive excitatory input from ON and OFF bipolar cells, which signal light increments (i.e., positive contrast) and decrements (i.e., negative contrast), respectively (26, 27, 39). We find that VG3 amacrine cells respond more strongly to looming than white looming because of a contrast-specific delay between excitation and inhibition. Whereas excitation and inhibition coincide during

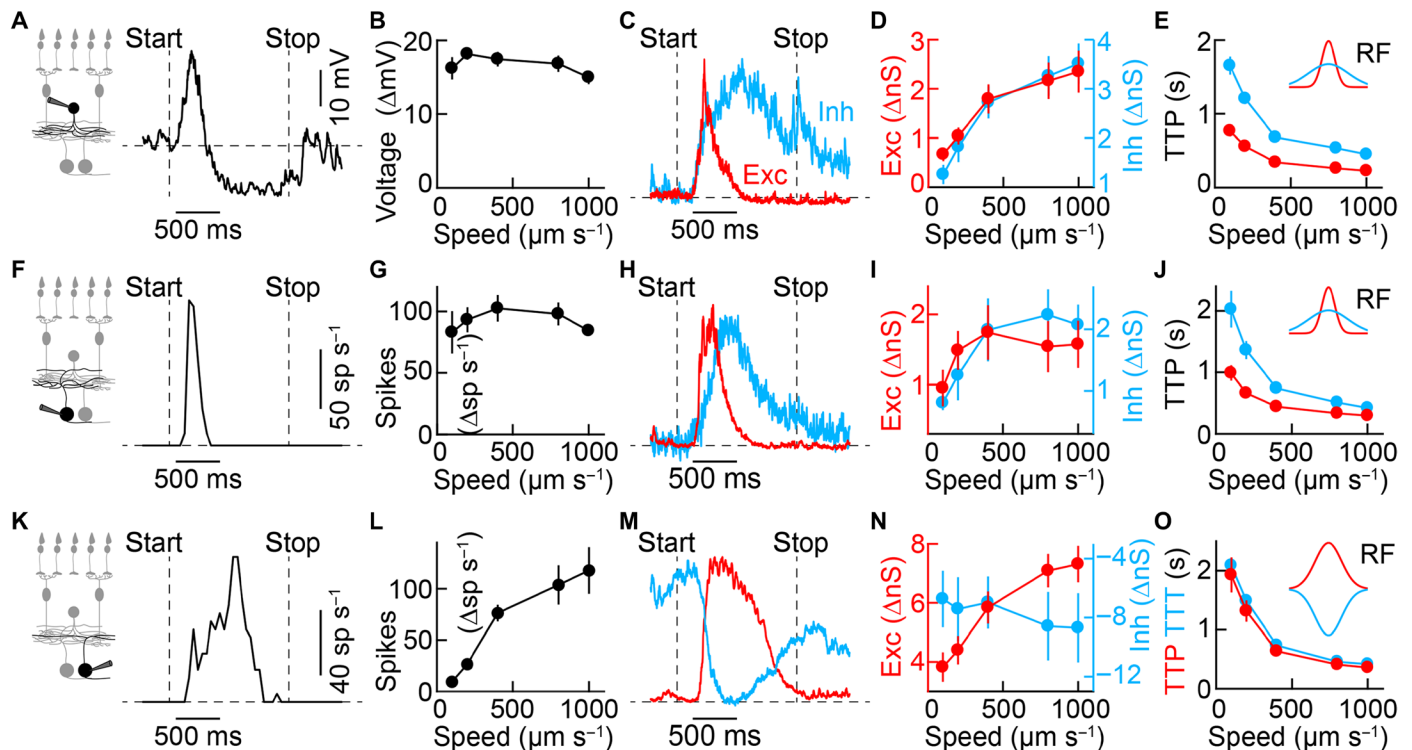


Fig. 4. Parallel parameter estimation in divergent circuits. (A and B) Representative trace (A) and summary data (B) of VG3 amacrine cell voltage responses to looming with varying speeds of expansion. The speed for all representative traces in this figure is $400 \mu\text{m s}^{-1}$. VG3 amacrine cells responses varied slightly with speed ($n = 8$ cells; $P = 0.038$, Friedman's test). (C to E) Representative traces (C) of excitatory and inhibitory inputs to VG3 amacrine cells and summary data of the amplitude (D) and latency (E; time to peak) of excitatory ($n = 11$ cells) and inhibitory ($n = 12$ cells) conductances at varying speeds of expansion. Excitation and inhibition increased in amplitude (excitation: $P = 9.3 \times 10^{-7}$; inhibition: $P = 5 \times 10^{-9}$; Friedman's test) and decreased in latency (excitation: $P = 1.3 \times 10^{-8}$; inhibition: $P = 2.8 \times 10^{-9}$; Friedman's test) with increasing stimulus speeds. Across speeds, inhibition was slower than excitation ($P = 1.5 \times 10^{-5}$, bootstrapping). (F and G) Representative trace (F) and summary data (G) for W3 spike responses, which did not vary significantly as a function of stimulus speed ($n = 5$ cells; $P = 0.31$, Friedman's test). (H to J) Representative traces (H) of excitatory and inhibitory inputs to W3 ganglion cells and summary data of the amplitude (I) and latency (J) of excitatory and inhibitory conductances at varying speeds of expansion ($n = 5$ cells). Inhibition, but not excitation, increased significantly in amplitude (excitation: $P = 0.14$; inhibition: $P = 0.032$; Friedman's test), and both decreased in latency (excitation: $P = 5 \times 10^{-4}$; inhibition: $P = 5 \times 10^{-4}$; Friedman's test) with increasing stimulus speed. Across speeds, inhibition was slower than excitation ($P = 0.01$, bootstrapping). (K and L) Representative trace (K) and summary data (L) for OFF α spike responses, increasing with stimulus speed ($n = 4$ cells; $P = 0.0086$, Friedman's test). (M to O) Representative traces (M) of excitatory and inhibitory inputs to OFF α ganglion cells and summary data of the amplitude (N) and latency (O) of excitatory and inhibitory conductances. Excitation increased and inhibition decreased in amplitude with increasing stimulus speed (excitation: $n = 4$ cells, $P = 0.0016$; inhibition: $n = 5$ cells, $P = 0.0037$; Friedman's test). The latency of excitation was not significantly different from that of inhibition ($P = 0.45$, bootstrapping), and both decreased with stimulus speed (excitation: $P = 0.003$; inhibition: $P = 5 \times 10^{-4}$; Friedman's test). Inset schematics in (E), (J), and (O) illustrate excitatory and inhibitory spatial receptive fields mapped with stationary dark spots (fig. S3). TTT, time to trough; TTP, time to peak; Exc, excitation; Inh, inhibition.

white looming, excitation precedes inhibition during looming (Fig. 1). This could either be due to differences in the size or arrangement of ON and OFF excitatory and inhibitory receptive fields, differences in the kinetics of the underlying mechanisms, or a combination of both. Maps constructed from responses to stationary stimuli indicate that OFF receptive fields of VG3 amacrine cells are smaller than their ON counterparts (22, 26, 27). The smaller OFF receptive fields explain the faster time to peak excitation for looming versus white looming (Fig. 1). However, the size ratios of the excitatory and inhibitory components do not differ significantly between the ON and OFF receptive fields of VG3 amacrine cells (ON: 0.53 ± 0.08 ; OFF: 0.56 ± 0.08 ; $P = 0.79$), and both are centrally aligned (26, 27). Therefore, we hypothesize that differences in the kinetics of receptive field mechanisms underlie the disparities in the relative timing of excitation and inhibition during looming versus white looming. The amacrine cells that inhibit VG3 amacrine cells during white looming may be driven by gap-junctional input from ON bipolar cells (40), whereas those that inhibit VG3 amacrine cells during looming

are likely driven by glutamate release from OFF bipolar cells. Identification of the amacrine cell types that inhibit VG3 amacrine cells will enable tests of this hypothesis.

Dendritic processing enhances feature selectivity

The dendrites of many neurons process synaptic inputs locally (41). Yet, the mechanisms of dendritic processing and its contributions to sensory feature detection remain mostly unknown (28, 29, 42). We combined patch-clamp recordings and two-photon calcium imaging to analyze how the dendrites of VG3 amacrine cells process visual threats. We found that dendritic processing enhances the looming preferences of VG3 amacrine cells via (i) thresholding and (ii) spatial segregation. The preference of VG3 amacrine cells for looming versus white looming was greater for dendritic calcium transients than voltage responses (Fig. 2). This was true across regions of interest (ROIs) with different baseline fluorescence, suggesting that it is not an effect of the calcium indicator (22). Instead, the higher selectivity of dendritic calcium signals likely reflects activation thresholds

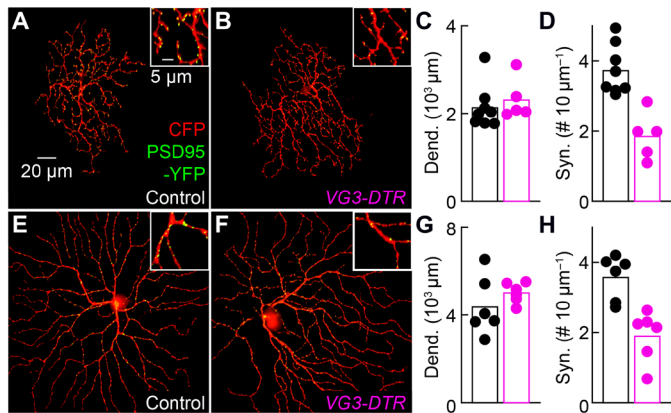


Fig. 5. VG3 removal reduces the density of excitatory synapses on W3 and OFF α ganglion cells. (A and B) Overview projections and excerpts (insets) of W3 dendrites biologically labeled with CFP and PSD95-YFP in VG3-DTR mice (B) and littermate controls (A). (C and D) Summary data show that W3 dendrite length was unchanged (C; control: $n = 8$ cells; VG3-DTR: $n = 5$ cells, $P = 0.35$, Mann-Whitney U test), but excitatory synapse density was reduced (D; $P = 0.0016$, by Wilcoxon rank-sum test) by VG3 amacrine cell removal. (E and F) Overview projections and excerpts of OFF α dendrites biologically labeled as in (A). (G and H) Summary data indicate that OFF α dendrite length was unchanged (G; control: $n = 6$ cells; VG3-DTR: $n = 6$ cells, $P = 0.24$, Mann-Whitney U test), but excitatory synapse density was reduced (H; $P = 0.0022$, Mann-Whitney U test) by VG3 amacrine cell removal.

of voltage-gated calcium channels, which are expressed in VG3 amacrine cells and contribute to transmitter release (27, 39). These activation thresholds sharpen the tuning of dendritic signals (43, 44). The cooperativity of calcium in promoting vesicle fusion likely further enhances looming preferences at the level of dendritic transmitter release (45). Thus, layered thresholding nonlinearities help VG3 dendrites detect visual threats.

VG3 dendrites limit the spread of synaptic inputs vertically and horizontally. Restrictions on vertical signal propagation segregate the processing of negative- and positive-contrast stimuli, which are relayed to different layers of their arbor by ON and OFF bipolar cells, respectively (22, 23). Vertical segregation enhances the looming preferences of the proximal layer of the VG3 arbor by preventing contamination from the white looming signals in the distal layer. In the VG3 plexus, the arbors of seven neighboring cells overlap at any point (26). Restrictions on horizontal signal spread (22, 23) increase the spatial resolution of looming signals and impose activity patterns with subcellular precision on the VG3 plexus irrespective of the cell identities of its constituent dendrites. Thus, spatial separation enhances the feature selectivity and topographic precision of looming responses in VG3 dendrites. Locally processing dendrites that receive input and provide output are a conserved feature of interneurons at the first three synapses of the visual system (i.e., horizontal cells, amacrine cells, and local interneurons of the thalamus) (18, 46, 47).

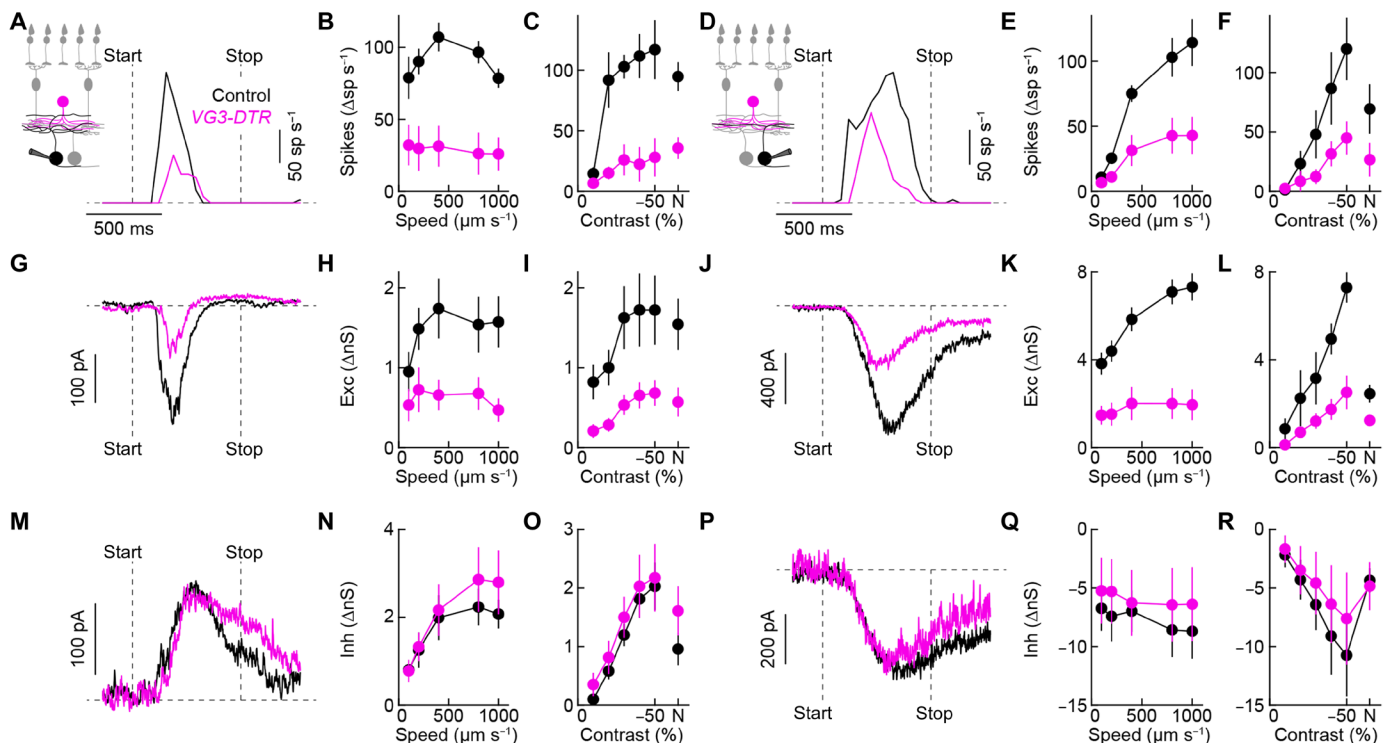


Fig. 6. Looming responses of W3 and OFF α ganglion cells depend on VG3 amacrine cells. (A to F) Representative traces and summary data of W3 (A to C) and OFF α (D to F) ganglion cell spike responses to looming. The speed for all representative traces in this figure is $800 \mu\text{m s}^{-1}$. Across stimulus speeds and contrasts (including luminance-neutral approach motion; N), spike responses of W3 (control: $n = 6$ cells; VG3-DTR: $n = 6$ cells; speed: $P = 4 \times 10^{-5}$; contrast: $P = 0.0017$, bootstrapping) and OFF α (control: $n = 4$ to 5 cells; VG3-DTR: $n = 6$ to 8 cells; speed: $P = 0.048$; contrast: $P = 0.047$, bootstrapping) ganglion cells were attenuated by VG3 amacrine cell removal. (G to L) Synaptic excitation was reduced by VG3 amacrine cell removal in W3 (G to I; control: $n = 5$ cells; VG3-DTR: $n = 7$ to 8 cells; speed: $P = 0.0024$; contrast: $P = 0.0021$, bootstrapping) and OFF α (J to L; control: $n = 4$ cells; VG3-DTR: $n = 4$ cells; speed: $P = 3 \times 10^{-5}$; contrast: $P = 0.0013$, bootstrapping) ganglion cells. (M to R) Looming-evoked synaptic inhibition was unaffected by VG3 amacrine cell removal in W3 (M to O; control: $n = 5$ cells; VG3-DTR: $n = 6$ to 7 cells; speed: $P = 0.77$; contrast: $P = 0.82$, bootstrapping) and OFF α (P to R; control: $n = 5$ cells; VG3-DTR: $n = 4$ cells; speed: $P = 0.91$; contrast: $P = 0.83$, bootstrapping) ganglion cells. The control data for different looming speeds in this figure are the same as those in Fig. 4. Exc, excitation; Inh, inhibition.

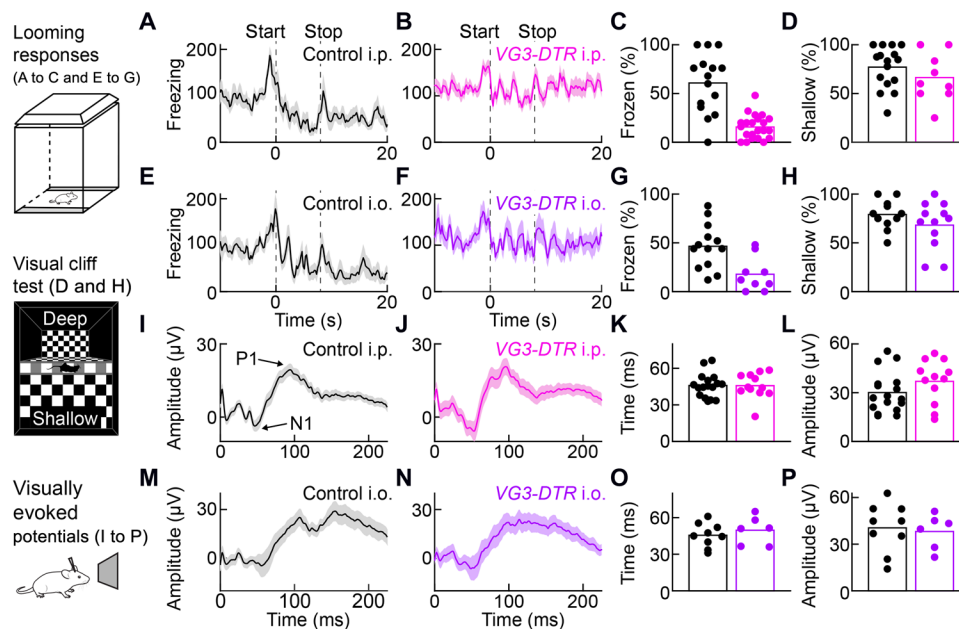


Fig. 7. Innate defensive responses to looming selectively depend on VG3 amacrine cells. (A and B) Lines (shaded areas) indicate the mean (\pm SEM) freezing score traces in response to looming for VG3-DTR mice (B; $n = 22$ mice) and control littermates (A; $n = 15$ mice) injected intraperitoneally with DT. (C) Summary data comparing the fraction of time frozen between these groups of mice (VG3-DTR intraperitoneal and Ctrl intraperitoneal) from stimulus onset to 20 s later (stimulus duration: 8 s). $P = 3.5 \times 10^{-5}$, Mann-Whitney U test. (D) Summary data of the performance of VG3-DTR intraperitoneal ($n = 9$ mice) and Ctrl intraperitoneal mice ($n = 15$ mice) in a visual cliff test. For each mouse, the percentage of shallow-side choices in 10 trials was measured. $P = 0.34$, Mann-Whitney U test. (E to H) Analogous to (A to D), comparing VG3-DTR mice and control littermates injected intraocularly with DT. For looming responses (E to G), VG3-DTR intraocular: $n = 9$ mice; Ctrl intraocular: $n = 13$ mice, $P = 0.0066$, Mann-Whitney U test. For the visual cliff test (H), VG3-DTR intraocular: $n = 12$ mice; Ctrl intraocular: $n = 11$ mice, $P = 0.35$, Mann-Whitney U test. (I and J) Lines (shaded areas) indicate the mean (\pm SEM) of visually evoked potentials recorded on skull electrodes above primary visual cortex in control (I; $n = 17$ mice) and VG3-DTR mice (J; $n = 12$ mice) 2 weeks after intraperitoneal injection of DT. (K and L) Summary data comparing implicit times (i.e., time to N1, $P = 0.89$, Mann-Whitney U test) and response amplitudes (i.e., P1-N1, $P = 0.16$, Mann-Whitney U test). (M to P) Analogous to (I) to (L) for control ($n = 9$ mice) and VG3-DTR mice ($n = 6$ mice) injected 2 weeks after bilateral intraocular injections of DT (implicit time: $P = 0.52$; amplitude: $P = 0.78$, Mann-Whitney U test). i.p., intraperitoneal; i.o., intraocular.

In each case, they enhance spatial resolution and enable individual neurons to make different contributions to parallel pathways that generate and propagate feature-selective signals.

Synaptic mechanisms of parallel parameter estimation in divergent circuits

Using optogenetics and anatomical circuit reconstructions, we show that VG3 amacrine cells form glutamatergic synapses with W3 and OFF α ganglion cells (Fig. 2) (26, 27, 35). Analyses of synaptic contacts in control mice (Fig. 2) (26) and synapse loss in VG3-DTR mice suggest that VG3 amacrine cells provide approximately half of the excitatory input to W3 and OFF α ganglion cells (Fig. 5); bipolar cells likely account for the remainder. W3 and OFF α ganglion cells combine shared excitation with categorically different inhibition to encode distinct parameters of looming (Fig. 4). During looming, W3 ganglion cells receive delayed inhibition (Fig. 4) from TH2 and other wide-field GABAergic amacrine cells (32, 35, 48). In this feedforward circuit, inhibitory and excitatory receptive fields have the same sign but differ in size (inhibition > excitation). Expanding motion, therefore, activates excitation and inhibition sequentially, and the response of W3 ganglion cells peaks at a critical stimulus size ($\sim 154 \mu\text{m}$ or $\sim 4.5^\circ$) independent of the speed of motion.

In contrast, OFF α ganglion cells receive tonic inhibition from AII amacrine cells, a narrow-field glycinergic ON responsive amacrine cell (31). During looming, inhibition from AII amacrine to OFF α ganglion cells is relieved (Fig. 4). In this crossover circuit, in-

hibitory and excitatory receptive fields have the opposite sign but similar size. As a result, OFF α ganglion cells' firing ramps up gradually during looming. Because excitation increases unopposed with stimulus speed, OFF α ganglion cells encode the speed of expanding motion. Together, these findings highlight the modularity of interneuron circuits in the retina, in which a single amacrine cell can distribute signals to multiple targets (i.e., divergence modularity), which combine them with input from other amacrine cells that make distinct and separable contributions to the overall computation (i.e., convergence modularity). Modular circuits transform signals from VG3 dendrites into parallel retinal outputs that encode the onset (or critical size) and speed of looming, respectively. It will be interesting to see how modular combinations of amacrine cells generate other feature representations in the retinal output and whether the principle of modularity generalizes to interneuron circuits elsewhere in the nervous system (49).

Behavioral significance of retinal feature detection

More than 60 years ago, Lettvin *et al.* (11) suggested that the frog retina explicitly reports salient events in the visual world to the frog brain. The behavioral significance of this retinal event detection, however, remained untested. Here, we show that VG3 amacrine cells and downstream ganglion cells signal looming and drive defensive responses by which mice evade aerial predators (Fig. 7). We find that W3 and OFF α ganglion cells signal different aspects of looming, critical size, and speed, respectively (Fig. 4). Similar response types have been

identified in the looming-sensitive tectal neurons of pigeons (17), indicating a conserved strategy in assessing predatory approaches.

In the taxonomy of visual motion, the first distinction is between (local) object motion and (global) self-generated motion (50). Looming is a specific form of object motion. VG3 amacrine cells distinguish object motion from self-generated motion and respond strongly to looming (Fig. 1) (26). Object motion sensitivity is tested with patterned stimuli that balance bright and dark regions (26, 32, 51), whereas looming consists of a radially expanding darkness (3, 50). The VG3 amacrine cell responses to balanced object motion and looming differ in their subcellular distribution. All VG3 dendrites respond to balanced object motion (22), whereas looming responses are restricted to the proximal layer of the VG3 arbor (Fig. 2). These stimulus-specific dendritic response distributions likely cause VG3 amacrine cells to activate (and suppress) different ganglion cell complements and contribute to the different behavioral responses to looming and balanced object motion.

We characterize the VG3-dependent looming responses of W3 and OFF α ganglion cells (Figs. 4 and 6). How other ganglion cell types, including suppressed-by-contrast ganglion cells, which receive stimulus-specific inhibition from VG3 amacrine cells (33, 34), respond to looming and how their responses are shaped by VG3 amacrine cells remains to be tested. Furthermore, how the VG3-dependent signals of W3, OFF α , and other ganglion cells are processed in downstream pathways that mediate defensive responses to looming is an exciting area for future investigation (5–10, 52). VG3 amacrine cells are conserved from rodents to primates (53, 54). We speculate that VG3 amacrine cells contribute to the innate defensive responses of infants to expanding shadows (55).

MATERIALS AND METHODS

Animals

To genetically target VG3 amacrine cells, we used bacterial artificial chromosome (BAC) transgenic mice expressing Cre recombinase under the control of regulatory sequences of the *Slc17a8* gene, which encodes VG3 (VG3-Cre mice) (39). We crossed VG3-Cre mice to a fluorescent reporter (*Ai9*) (56) and optogenetic actuator (*Ai32*) (57) 57 lines to enable targeted recording and connectivity mapping. For subcellular analyses of visual processing by two-photon imaging, we crossed VG3-Cre mice to a GCaMP6f reporter line (*Ai148*) (22, 58). To selectively remove VG3 amacrine cells, we crossed VG3-Cre mice to a line expressing the DT receptor in a Cre-dependent manner (*DTR* mice) (59). We injected double-positive offspring (VG3-DTR mice) and their Cre⁻ and/or DTR⁻ littermates (control mice) intraperitoneally or intraocularly (i.o.) with DT. For intraperitoneal administration, mice were injected four times with DT (1 mg per 50 g body weight) once a day every other day starting at postnatal day 30 (P30). For i.o. administration, mice were injected once with 10 to 15 ng of DT in each eye at P30. Experiments were performed 1 to 2 weeks after the last injection. All procedures in this study were approved by the Animal Studies Committee of Washington University School of Medicine (protocol nos. 20170033 and 20-0055) and performed in compliance with the National Institutes of Health Guide for the Care and Use of Laboratory Animals.

Patch-clamp recordings and optogenetics

We obtained patch-clamp recordings of VG3 amacrine cells and W3 and OFF α ganglion cells in retinal flat-mount preparations. Retinas from dark-adapted (>2 hours) mice were isolated under infrared

illumination, mounted on membrane disk (Anodisc, Whatman), and continually perfused (~ 7 ml min⁻¹) with warm ($\sim 33^\circ\text{C}$) bicarbonate-buffered mouse artificial cerebrospinal fluid (mACSF_{NaHCO₃}) containing 125 mM NaCl, 2.5 mM KCl, 1 mM MgCl₂, 1.25 mM NaH₂PO₄, 2 mM CaCl₂, 20 mM glucose, 26 mM NaHCO₃, and 0.5 mM L-glutamine equilibrated with 95% O₂/5% CO₂. For optogenetics, L-2-amino-4-phosphonobutyric acid (AP4; 20 mM) and (S)-1-(2-Amino-2-carboxyethyl)-3-(2-carboxy-5-phenylthiophene-3-yl-methyl)-5-methylpyrimidine-2,4-dione (ACET) (10 mM) were added to mACSF_{NaHCO₃} to block transmission of photoreceptor signals to ON and OFF bipolar cells, respectively. The intracellular solution for current-clamp recordings contained 125 mM K-gluconate, 10 mM NaCl, 1 mM MgCl₂, 10 mM EGTA, 5 mM Hepes, 5 mM adenosine 5'-triphosphate-Na, and 0.1 mM guanosine 5'-triphosphate-Na (pH adjusted to 7.2 with KOH). The intracellular solution for voltage-clamp recordings contained 120 mM Cs-gluconate, 1 mM CaCl₂, 1 mM MgCl₂, 10 mM Na-Hepes, 11 mM EGTA, 10 mM tetraethylammonium (TEA)-Cl, and 2 mM Qx314 (pH adjusted to 7.2 with CsOH). Patch pipettes had resistances of 4 to 7 M Ω (borosilicate glass). Signals were amplified with a Multiclamp 700B amplifier (Molecular Devices), filtered at 3 kHz (8-pole Bessel low-pass), and sampled at 10 kHz (Digidata 1440A, Molecular Devices). In voltage-clamp recordings, series resistance (10 to 15 M Ω) was compensated electronically by $\sim 75\%$. Excitatory postsynaptic currents and inhibitory postsynaptic currents were isolated by holding cells at the reversal potential of inhibitory (-60 mV) and excitatory (0 mV) conductances, respectively. In current-clamp recordings, no bias currents were injected. We targeted VG3 amacrine cells under two-photon guidance and recorded W3 and OFF α ganglion cells under conventional infrared illumination. We identified ganglion cell types and confirmed VG3 amacrine cell identity by including Alexa 488 or Alexa 568 (0.1 mM) in the intracellular solution and acquiring two-photon image stacks at the end of each recording.

Visual stimuli were presented on an organic light-emitting display (eMagin) and projected onto the photoreceptor side of the dorsal retina via the substage condenser. In looming stimuli, a 20- μm (0.6 $^\circ$) disk appeared on a gray background, remained stable for 1 s, then expanded to 600 μm (17.6 $^\circ$), remained at this size for 1 s, and disappeared (Fig. 1). The contrast of the disk relative to the background was varied (-100 to 100% Weber contrast), as was the speed of expansion (100 to 1000 $\mu\text{m s}^{-1}$ or 2.9 to 29 $^\circ\text{s}^{-1}$). In receding stimuli, the inverse sequence to looming stimuli was shown. In luminance-neutral approaching motion stimuli, the summed intensity in a 600- μm -diameter disk was kept constant as the central disk expanded (Fig. 6 and fig. S1). Response amplitudes were measured as the mean of the respective traces in 100-ms windows centered on their extrema.

To activate Channelrhodopsin-2 in VG3-Cre *Ai32* retinas, light stimuli were presented from the ganglion cell side through a 20 \times 0.95 numerical aperture (NA) water immersion objective. Light from a mercury bulb (Olympus) was bandpass-filtered (426 to 446 nm, Chroma) and attenuated by neutral density filters (Chroma). In targeted recordings from VG3 amacrine cells, we previously identified an optogenetic stimulus intensity (3.15×10^{-4} W mm⁻²) that matches photoreceptor-mediated light responses of VG3 amacrine cells (33). Stimulus timing was controlled by a Uniblitz shutter (Vincent Associates).

Two-photon calcium imaging

The retina was isolated and flat-mounted as for patch-clamp recordings. A custom-built upright two-photon microscope (Scientifica)

controlled by the Scanimage r3.8 MATLAB toolbox was used to acquire images via a DAQ NI PCI6110 data acquisition board (National Instruments). In *VG3-Cre Ai148* mice, GCaMP6f was excited with a Mai-Tai laser (Spectra-Physics) tuned to 930 nm (laser power: <7 mW at the sample), and fluorescence emission was collected via a 60 × 1.0 NA water immersion objective (Olympus) filtered through consecutive 450-nm long-pass (Thorlabs) and 513- to 528-nm band-pass filters (Chroma). This blocked visual stimulus light (385 nm) from reaching the PMT. We acquired images throughout this study at 9.5 Hz with a pixel density of 4.7 pixels μm^{-2} . Imaging depths were registered by their relative distances to the borders between the inner plexiform layer (IPL) and the inner nuclear layer (IPL depth: 0%) and between the IPL and the ganglion cell layer (IPL depth: 100%). Borders were detected in transmitted light images. Scan fields at different IPL depths were imaged in pseudorandom order, and for each scan, the retina was adapted to the laser light for 30 s before the presentation of visual stimuli. Throughout the experiments, retinas were perfused at $\sim 7 \text{ ml min}^{-1}$ with 33°C mACSF_{NaHCO₃} equilibrated with 95% O₂/5% CO₂. Images were denoised, registered, and segmented into functionally distinct ROIs as described previously (22).

Visual stimuli were presented from a ultraviolet E4500 MKII PLUS II projector illuminated by a 385-nm light-emitting diode (EKB Technologies) and focused onto the photoreceptors of the ventral retina, where S-opsin dominates (60), via the substage condenser. We used neutral density filters (Thorlabs, FW102CNEB) to attenuate the output of the projector. Stimuli were centered on the two-photon scan field, and their average intensity kept constant at ~ 1600 S-opsin isomerizations S-cone⁻¹ s⁻¹. The parameters of looming, receding, and white looming stimuli were identical to those used for patch-clamp recordings. Stimulus speeds were limited to 800 $\mu\text{m s}^{-1}$ (24° s⁻¹). In addition, we presented stationary stimuli, in which the light intensity was square-wave modulated (1.5 s ON and 1.5 s OFF) in a 100- μm disk. Stationary stimuli were interleaved with looming, receding, and white looming stimuli to facilitate comparisons of the responses of individual ROIs. We calculated the following preference indices: Preference index (loom versus recede) = $(L - R)/(L + R)$, where L and R indicate responses to looming and receding, respectively; Preference index (black versus white)_{expanding} = $(L - WL)/(L + WL)$, where L and WL indicate responses to looming and white looming, respectively; and Preference index (black versus white)_{stationary} = $(\text{OFF} - \text{ON})/(\text{OFF} + \text{ON})$, where OFF and ON indicate responses to light decrements and increments, respectively, of stationary disks.

Anatomy

To map excitatory connections of VG3 amacrine cells with W3 and OFF α ganglion cells, we biolistically labeled flat-mounted retinas with cytosolic tdTomato and PSD95-YFP. Retinas were isolated in Hepes-buffered mouse artificial cerebrospinal fluid (mACSF_{Hepes})—containing 119 mM NaCl, 2.5 mM KCl, 2.5 mM CaCl₂, 1.3 mM MgCl₂, 1 mM NaH₂PO₄, 11 mM glucose, and 20 mM Hepes (pH adjusted to 7.37 with NaOH)—and mounted on membrane disks (HABGO1300, Millipore). Gold particles (1.6- μm diameter; Bio-Rad) were coated with plasmids encoding tdTomato and PSD95-YFP as previously described and were delivered to ganglion cells from a helium-pressurized gun (Bio-Rad) at 40 psi. Retinas were then incubated in a humid oxygenated chamber at 33° to 35°C for 14 to 18 hours in mACSF_{Hepes}, fixed for 30 min in 4% paraformaldehyde in mACSF_{Hepes}, and washed in PBS (three times, 10 min) before mounting and imaging.

Confocal image stacks (voxel size: 0.103 μm x/y , 0.3 μm z) of biolistically labeled W3 and OFF α ganglion cells were acquired on an Fv1000 laser scanning microscope (Olympus) using a 60 × 1.35 NA oil immersion objective. We skeletonized dendrites and synapses identified in confocal image stacks using previously described algorithms (36) to measure dendrite lengths and synapse densities (Fig. 5). To determine the fraction of excitatory synapses on OFF α dendrites apposed by VG3 boutons (Fig. 3), we separately masked OFF α dendrites, PSD95-YFP puncta, and VG3 dendrites in Amira (Thermo Fisher Scientific). Excitatory synapses on OFF α dendrites formed by VG3 amacrine cells were defined as PSD95 clusters with a center of mass within 0.5 μm of a VG3 dendrite. We confirmed that varying this distance from 0.25 to 1 μm did not qualitatively change the results. We repeated the same analysis for each cell in image stacks in which the amacrine cell channel was rotated by 90° to compare the fraction of PSD95-YFP apposed by VG3 dendrites to that caused by random signal overlap.

To analyze the number and distribution of VG3 neurons, we stained retinal flat mounts and vibratome slices (thickness: 100 μm) of different brain regions in *VG3-Cre Ai9* mice and *VG3-DTR Ai9* mice were injected with DT intraperitoneally or i.o. for tdTomato (primary antibody: rabbit anti-DsRed, 1:1000; BD Biosciences, RRID:AB_394264; secondary antibody: donkey anti-rabbit immunoglobulin G Alexa 568, 1:1000; Thermo Fisher Scientific, RRID:AB_253401) and obtained confocal images stacks (voxel size: 0.62 to 1.24 μm x/y and 1 to 5 μm z) on an Fv1000 laser scanning microscope (Olympus) using 20 × 1.35 NA oil immersion and 10× objective.

Visually evoked potential recordings

We recorded flash visually evoked potentials on the UTAS-E3000 Visual Electrodiagnostic System (LKC Technologies). Mice were dark-adapted for >2 hours and anesthetized with ketamine (80 mg kg⁻¹) and xylazine (15 mg kg⁻¹) cocktail under dim red light. We dilated pupils with 1% atropine sulfate and applied hypromellose ophthalmic ointment (Gonak) to the cornea. A platinum wire (diameter: 0.25 mm; Alfa Aesar) was inserted subcutaneously over the right side of visual cortex (~ 8 mm from the midline), and mice were placed on a heating pad with a reference needle electrode pinned in the left ear and a ground needle electrode inserted under the tail skin. The platinum wire was connected to the system via a clamp electrode. Mice were in the complete darkness for 3 min before recordings. For each recording, responses of 80 repeated flashes (intensity: 2 cdS m⁻², frequency: 2 Hz) were averaged.

Behavior

To analyze responses to looming stimuli, mice were placed in a 45 cm by 27 cm by 31 cm box (width × depth × height) with three opaque walls and one transparent wall (Fig. 1A). We recorded videos through the transparent wall with a universal serial bus (USB) camera (720p, ELP, or C310, Logitech) and presented stimuli on an LCD monitor (32 cm by 24 cm display area; mean stimulus intensity: ~ 1600 M-opsin isomerizations M-cone⁻¹ s⁻¹; refresh rate: 60 Hz), which formed the ceiling of the box. Looming stimuli consisted of a 2° (diameter) dark disk on a gray background that expanded to a 20° in 0.25 to 1 s (18 to 72° s⁻¹), remained this size for 0.25 s, before starting again at 2° for a sequence that repeated 20 times without gaps (Fig. 1A). Stimuli were started when mice entered the center of the arena. Alternatively, mice were shown a bright disk expanding on a gray background or a dark disk shrinking

with kinetic and size parameters matching the looming stimulus (Fig. 1, B and C). Mice were acclimatized to the behavioral arena for at least 5 min before stimulus presentation. Because mice habituate to these stimuli, only the first presentation of each stimulus for an animal was included in our analysis. We recorded and analyzed mouse behavior automatically using ANY-maze tracking software (Stoelting). Consistent with previous studies (8), we defined mice as frozen when the freezing score was <30. We report the percentage of time mice spent in this state from stimulus onset to 20 s later as a summary parameter. We confirmed that varying the freezing score threshold ($\pm 50\%$) did not qualitatively change our results.

Visual cliff tests were performed on a 56-cm by 41-cm platform (width \times depth) with a 3.8-cm by 1.7-cm ridge (height \times width) across its center. On one side of the ridge, a checkered pattern was immediately below the platform (i.e., the shallow side), and on the other side, an identical checkered pattern was 61 cm below the platform (i.e., the cliff side). Mice were placed on the ridge and filmed via a USB camera (720p, ELP, or C310, Logitech). For each mouse, we measured the percentage of shallow-side choices in at least 10 trials.

Statistical analyses

Data were analyzed using scripts written in MATLAB (The MathWorks). The code will be made available upon request. Summary data are presented as means \pm SEM. Nonparametric tests (Mann-Whitney *U*, Wilcoxon signed-rank, Friedman's, and Kruskal-Wallis) and bootstrapping were used to compare data from different experimental groups as specified in the figure legends. Statistical significance was considered when $P < 0.05$.

SUPPLEMENTARY MATERIALS

Supplementary material for this article is available at <http://advances.sciencemag.org/cgi/content/full/6/47/eabc9920/DC1>

[View/request a protocol for this paper from Bio-protocol.](#)

REFERENCES AND NOTES

- H. Fotowat, F. Gabbiani, Collision detection as a model for sensory-motor integration. *Annu. Rev. Neurosci.* **34**, 1–19 (2011).
- M. Y. Peek, G. M. Card, Comparative approaches to escape. *Curr. Opin. Neurobiol.* **41**, 167–173 (2016).
- M. Yilmaz, M. Meister, Rapid innate defensive responses of mice to looming visual stimuli. *Curr. Biol.* **23**, 2011–2015 (2013).
- G. De Franceschi, T. Vivattanasarn, A. B. Saleem, S. G. Solomon, Vision guides selection of freeze or flight defense strategies in mice. *Curr. Biol.* **26**, 2150–2154 (2016).
- C. Shang, Z. Liu, Z. Chen, Y. Shi, Q. Wang, S. Liu, D. Li, P. Cao, A parvalbumin-positive excitatory visual pathway to trigger fear responses in mice. *Science* **348**, 1472–1477 (2015).
- C. Shang, Z. Chen, A. Liu, Y. Li, J. Zhang, B. Qu, F. Yan, Y. Zhang, W. Liu, Z. Liu, X. Guo, D. Li, Y. Wang, P. Cao, Divergent midbrain circuits orchestrate escape and freezing responses to looming stimuli in mice. *Nat. Commun.* **9**, 1232 (2018).
- L. Huang, T. Yuan, M. Tan, Y. Xi, Y. Hu, Q. Tao, Z. Zhao, J. Zheng, Y. Han, F. Xu, M. Luo, P. J. Sollars, M. Pu, G. E. Pickard, K.-F. So, C. Ren, A retinographic projection regulates serotonergic activity and looming-evoked defensive behaviour. *Nat. Commun.* **8**, 14908 (2017).
- P. Wei, N. Liu, Z. Zhang, X. Liu, Y. Tang, X. He, B. Wu, Z. Zhou, Y. Liu, J. Li, Y. Zhang, X. Zhou, L. Xu, L. Chen, G. Bi, X. Hu, F. Xu, L. Wang, Processing of visually evoked innate fear by a non-canonical thalamic pathway. *Nat. Commun.* **6**, 6756 (2015).
- L. D. Salay, N. Ishiko, A. D. Huberman, A midline thalamic circuit determines reactions to visual threat. *Nature* **557**, 183–189 (2018).
- D. A. Evans, A. V. Stempel, R. Vale, S. Ruehle, Y. Lefler, T. Branco, A synaptic threshold mechanism for computing escape decisions. *Nature* **558**, 590–594 (2018).
- J. Y. Lettvin, H. R. Maturana, W. S. McCulloch, W. H. Pitts, What the frog's eye tells the frog's brain. *Proc. IRE* **47**, 1940–1951 (1959).
- H. Barlow, Possible Principles Underlying the Transformations of Sensory Messages in *Sensory Communication* (MIT Press, 1961); 10.7551/mitpress/9780262518420.003.0013.
- T. Gollisch, M. Meister, Eye smarter than scientists believed: Neural computations in circuits of the retina. *Neuron* **65**, 150–164 (2010).
- J. R. Sanes, R. H. Masland, The types of retinal ganglion cells: Current status and implications for neuronal classification. *Annu. Rev. Neurosci.* **38**, 221–246 (2015).
- K. Yoshida, D. Watanabe, H. Ishikane, M. Tachibana, I. Pastan, S. Nakanishi, A key role of starburst amacrine cells in originating retinal directional selectivity and optokinetic eye movement. *Neuron* **30**, 771–780 (2001).
- K. Yonehara, M. Fiscella, A. Drinnenberg, F. Esposti, S. Trenholm, J. Krol, F. Franke, B. G. Scherf, A. Kusnyerik, J. Müller, A. Szabo, J. Jüttner, F. Cordoba, A. P. Reddy, J. Némethy, Z. Z. Nagy, F. Munier, A. Hierlemann, B. Roska, Congenital nystagmus gene FRMD7 is necessary for establishing a neuronal circuit asymmetry for direction selectivity. *Neuron* **89**, 177–193 (2016).
- H. Sun, B. J. Frost, Computation of different optical variables of looming objects in pigeon nucleus reticulatus neurons. *Nat. Neurosci.* **1**, 296–303 (1998).
- J. S. Diamond, Inhibitory interneurons in the retina: Types, circuitry, and function. *Annu. Rev. Vis. Sci.* **3**, 1–24 (2017).
- M. Helmstaedter, K. L. Briggman, S. C. Turaga, V. Jain, H. S. Seung, W. Denk, Connectomic reconstruction of the inner plexiform layer in the mouse retina. *Nature* **500**, 168–174 (2013).
- W. Yan, M. A. Laboulaye, N. M. Tran, I. E. Whitney, I. Benhar, J. R. Sanes, Mouse retinal cell atlas: Molecular identification of over sixty amacrine cell types. *J. Neurosci.* **40**, 5177–5195 (2020).
- Z. J. Huang, A. Paul, The diversity of GABAergic neurons and neural communication elements. *Nat. Rev. Neurosci.* **20**, 563–572 (2019).
- J.-C. Hsiang, K. P. Johnson, L. Madisen, H. Zeng, D. Kerschensteiner, Local processing in neurites of VGLUT3-expressing amacrine cells differentially organizes visual information. *eLife* **6**, e31307 (2017).
- M. Chen, S. Lee, Z. J. Zhou, Local synaptic integration enables ON-OFF asymmetric and layer-specific visual information processing in vGluT3 amacrine cell dendrites. *Proc. Natl. Acad. Sci. U.S.A.* **114**, 11518–11523 (2017).
- A. S. Mauss, A. Vlasits, A. Borst, M. Feller, Visual circuits for direction selectivity. *Annu. Rev. Neurosci.* **40**, 211–230 (2017).
- W. Wei, Neural mechanisms of motion processing in the mammalian retina. *Annu. Rev. Vis. Sci.* **4**, 165–192 (2018).
- T. Kim, F. Soto, D. Kerschensteiner, An excitatory amacrine cell detects object motion and provides feature-selective input to ganglion cells in the mouse retina. *eLife* **4**, e08025 (2015).
- S. Lee, L. Chen, M. Chen, M. Ye, R. P. Seal, Z. J. Zhou, An unconventional glutamatergic circuit in the retina formed by vGluT3 amacrine cells. *Neuron* **84**, 708–715 (2014).
- T. Euler, P. B. Detwiler, W. Denk, Directionally selective calcium signals in dendrites of starburst amacrine cells. *Nature* **418**, 845–852 (2002).
- W. N. Grimes, J. Zhang, C. W. Graydon, B. Kachar, J. S. Diamond, Retinal parallel processors: More than 100 independent microcircuits operate within a single interneuron. *Neuron* **65**, 873–885 (2010).
- J. A. Bae, S. Mu, J. S. Kim, N. L. Turner, I. Tartavull, N. Kemnitz, C. S. Jordan, A. D. Norton, W. M. Silversmith, R. Prentki, M. Sorek, C. David, D. L. Jones, D. Bland, A. L. R. Sterling, J. Park, K. L. Briggman, H. S. Seung, Eyewirers, Digital museum of retinal ganglion cells with dense anatomy and physiology. *Cell* **173**, 1293–1306.e19 (2018).
- T. A. Münch, R. A. da Silveira, S. Siegert, T. J. Viney, G. B. Awatramani, B. Roska, Approach sensitivity in the retina processed by a multifunctional neural circuit. *Nat. Neurosci.* **12**, 1308–1316 (2009).
- Y. Zhang, I.-J. Kim, J. R. Sanes, M. Meister, The most numerous ganglion cell type of the mouse retina is a selective feature detector. *Proc. Natl. Acad. Sci. U.S.A.* **109**, E2391–E2398 (2012).
- N.-W. Tien, T. Kim, D. Kerschensteiner, Target-specific glycinergic transmission from VGLUT3-expressing amacrine cells shapes suppressive contrast responses in the retina. *Cell Rep.* **15**, 1369–1375 (2016).
- S. Lee, Y. Zhang, M. Chen, Z. J. Zhou, Segregated glycine-glutamate co-transmission from vGluT3 amacrine cells to contrast-suppressed and contrast-enhanced retinal circuits. *Neuron* **90**, 27–34 (2016).
- A. Krishnaswamy, M. Yamagata, X. Duan, Y. K. Hong, J. R. Sanes, Sidekick 2 directs formation of a retinal circuit that detects differential motion. *Nature* **524**, 466–470 (2015).
- D. Kerschensteiner, J. L. Morgan, E. D. Parker, R. M. Lewis, R. O. L. Wong, Neurotransmission selectively regulates synapse formation in parallel circuits in vivo. *Nature* **460**, 1016–1020 (2009).
- N.-W. Tien, F. Soto, D. Kerschensteiner, Homeostatic plasticity shapes cell-type-specific wiring in the retina. *Neuron* **94**, 656–665.e4 (2017).
- H. Okawa, L. Della Santina, G. W. Schwartz, F. Rieke, R. O. L. Wong, Interplay of cell-autonomous and nonautonomous mechanisms tailors synaptic connectivity of converging axons in vivo. *Neuron* **82**, 125–137 (2014).
- W. N. Grimes, R. P. Seal, N. Oesch, R. H. Edwards, J. S. Diamond, Genetic targeting and physiological features of VGLUT3+ amacrine cells. *Vis. Neurosci.* **28**, 381–392 (2011).

40. K. Farrow, M. Teixeira, T. Szikra, T. J. Viney, K. Balint, K. Yonehara, B. Roska, Ambient illumination toggles a neuronal circuit switch in the retina and visual perception at cone threshold. *Neuron* **78**, 325–338 (2013).
41. T. Branco, M. Häusser, The single dendritic branch as a fundamental functional unit in the nervous system. *Curr. Opin. Neurobiol.* **20**, 494–502 (2010).
42. H. Jia, N. L. Rochefort, X. Chen, A. Konnerth, Dendritic organization of sensory input to cortical neurons in vivo. *Nature* **464**, 1307–1312 (2010).
43. J. S. Isaacson, M. Scanziani, How inhibition shapes cortical activity. *Neuron* **72**, 231–243 (2011).
44. N. Oesch, T. Euler, W. R. Taylor, Direction-selective dendritic action potentials in rabbit retina. *Neuron* **47**, 739–750 (2005).
45. F. A. Dodge Jr., R. Rahamimoff, Co-operative action of calcium ions in transmitter release at the neuromuscular junction. *J. Physiol.* **193**, 419–432 (1967).
46. J. L. Morgan, J. W. Lichtman, An individual interneuron participates in many kinds of inhibition and innervates much of the mouse visual thalamus. *Neuron* **106**, 468–481.e2 (2020).
47. C. A. Chapot, T. Euler, T. Schubert, How do horizontal cells “talk” to cone photoreceptors? Different levels of complexity at the cone-horizontal cell synapse. *J. Physiol.* **595**, 5495–5506 (2017).
48. T. Kim, D. Kerschensteiner, Inhibitory control of feature selectivity in an object motion sensitive circuit of the retina. *Cell Rep.* **19**, 1343–1350 (2017).
49. C. K. Pfeffer, M. Xue, M. He, Z. J. Huang, M. Scanziani, Inhibition of inhibition in visual cortex: The logic of connections between molecularly distinct interneurons. *Nat. Neurosci.* **16**, 1068–1076 (2013).
50. B. J. Frost, A taxonomy of different forms of visual motion detection and their underlying neural mechanisms. *Brain Behav. Evol.* **75**, 218–235 (2010).
51. B. P. Ölveczky, S. A. Baccus, M. Meister, Segregation of object and background motion in the retina. *Nature* **423**, 401–408 (2003).
52. K. Reinhard, C. Li, Q. Do, E. G. Burke, S. Heynderickx, K. Farrow, A projection specific logic to sampling visual inputs in mouse superior colliculus. *eLife* **8**, e50697 (2019).
53. S. Haverkamp, H. Wässle, Characterization of an amacrine cell type of the mammalian retina immunoreactive for vesicular glutamate transporter 3. *J. Comp. Neurol.* **468**, 251–263 (2004).
54. Y.-R. Peng, K. Shekhar, W. Yan, D. Herrmann, A. Sappington, G. S. Bryman, T. van Zyl, M. T. H. Do, A. Regev, J. R. Sanes, Molecular classification and comparative taxonomies of foveal and peripheral cells in primate retina. *Cell* **176**, 1222–1237.e22 (2019).
55. W. Ball, E. Tronick, Infant responses to impending collision: Optical and real. *Science* **171**, 818–820 (1971).
56. L. Madisen, T. A. Zwingman, S. M. Sunkin, S. W. Oh, H. A. Zariwala, H. Gu, L. L. Ng, R. D. Palmiter, M. J. Hawrylycz, A. R. Jones, E. S. Lein, H. Zeng, A robust and high-throughput Cre reporting and characterization system for the whole mouse brain. *Nat. Neurosci.* **13**, 133–140 (2010).
57. L. Madisen, T. Mao, H. Koch, J.-M. Zhuo, A. Berenyi, S. Fujisawa, Y.-W. A. Hsu, A. J. Garcia III, X. Gu, S. Zanella, J. Kidney, H. Gu, Y. Mao, B. M. Hooks, E. S. Boyden, G. Buzsáki, J. M. Ramirez, A. R. Jones, K. Svoboda, X. Han, E. E. Turner, H. Zeng, A toolbox of Cre-dependent optogenetic transgenic mice for light-induced activation and silencing. *Nat. Neurosci.* **15**, 793–802 (2012).
58. T. L. Daigle, L. Madisen, T. A. Hage, M. T. Valley, U. Knoblich, R. S. Larsen, M. M. Takeno, L. Huang, H. Gu, R. Larsen, M. Mills, A. Bosma-Moody, L. A. Siverts, M. Walker, L. T. Graybuck, Z. Yao, O. Fong, T. N. Nguyen, E. Garren, G. H. Lenz, M. Chavarha, J. Pendergraft, J. Harrington, K. E. Hirokawa, J. A. Harris, P. R. Nicovich, M. J. McGraw, D. R. Ollerenshaw, K. A. Smith, C. A. Baker, J. T. Ting, S. M. Sunkin, J. Lecoq, M. Z. Lin, E. S. Boyden, G. J. Murphy, N. M. da Costa, J. Waters, L. Li, B. Tasic, H. Zeng, A suite of transgenic driver and reporter mouse lines with enhanced brain-cell-type targeting and functionality. *Cell* **174**, 465–480.e22 (2018).
59. T. Buch, F. L. Heppner, C. Tertilt, T. J. A. J. Heinen, M. Kremer, F. T. Wunderlich, S. Jung, A. Waisman, A Cre-inducible diphtheria toxin receptor mediates cell lineage ablation after toxin administration. *Nat. Methods* **2**, 419–426 (2005).
60. Y. V. Wang, M. Weick, J. B. Demb, Spectral and temporal sensitivity of cone-mediated responses in mouse retinal ganglion cells. *J. Neurosci.* **31**, 7670–7681 (2011).

Acknowledgments: We thank all members of the Kerschensteiner laboratory for discussions throughout the project; B. Wang and L. Zhao for expert technical assistance; and M. Bagnall, M. Kerschensteiner, J.L. Morgan, and F. Soto for critical reading of the manuscript. **Funding:** This work was supported by the NIH (EY023341, EY026978, EY027411, and EY030623 to D.K. and the Vision Core grant EY0268), the Grace Nelson Lacy Research Fund (director: D.K.), and an unrestricted grant to the Department of Ophthalmology and Visual Sciences from Research to Prevent Blindness. **Author contributions:** T.K. and D.K. conceived of this study. T.K. and K.P.J. performed patch-clamp recordings. T.K. and D.K. performed anatomy experiments. J.-C.H. performed two-photon imaging experiments. T.K., N.S., and D.K. performed behavioral experiments. All authors analyzed data and contributed to the experimental design. D.K. wrote the manuscript with input from all authors. **Competing interests:** The authors declare that they have no competing interests. **Data and materials availability:** All data needed to evaluate the paper are present in the paper and/or the Supplementary Materials. Additional data related to this paper may be requested from the authors.

Submitted 25 May 2020

Accepted 1 October 2020

Published 18 November 2020

10.1126/sciadv.abc9920

Citation: T. Kim, N. Shen, J.-C. Hsiang, K. Johnson, D. Kerschensteiner, Dendritic and parallel processing of visual threats in the retina control defensive responses. *Sci. Adv.* **6**, eabc9920 (2020).

Dendritic and parallel processing of visual threats in the retina control defensive responses

T. Kim, N. Shen, J.-C. Hsiang, K.P. Johnson and D. Kerschensteiner

Sci Adv **6** (47), eabc9920.

DOI: 10.1126/sciadv.abc9920

ARTICLE TOOLS

<http://advances.sciencemag.org/content/6/47/eabc9920>

SUPPLEMENTARY MATERIALS

<http://advances.sciencemag.org/content/suppl/2020/11/16/6.47.eabc9920.DC1>

REFERENCES

This article cites 59 articles, 6 of which you can access for free
<http://advances.sciencemag.org/content/6/47/eabc9920#BIBL>

PERMISSIONS

<http://www.sciencemag.org/help/reprints-and-permissions>

Use of this article is subject to the [Terms of Service](#)

Science Advances (ISSN 2375-2548) is published by the American Association for the Advancement of Science, 1200 New York Avenue NW, Washington, DC 20005. The title *Science Advances* is a registered trademark of AAAS.

Copyright © 2020 The Authors, some rights reserved; exclusive licensee American Association for the Advancement of Science. No claim to original U.S. Government Works. Distributed under a Creative Commons Attribution NonCommercial License 4.0 (CC BY-NC).